



How perfluoroalkyl substances modify fluorinated self-assembled monolayer architectures: An electrochemical and computational study



Giulia Moro ^{a, b, c, *}, Cedrix J. Dongmo Fomthum ^a, Marco Spinaci ^a, Ettore Martini ^a, Dafne Cimino ^d, Eleonora Balliana ^d, Peter Lieberzeit ^e, Flavio Romano ^a, Achille Giacometti ^{a, f}, Rui Campos ^{b, c}, Karolien De Wael ^{b, c}, Ligia Maria Moretto ^a

^a Department of Molecular Sciences and Nanosystems, Ca' Foscari University of Venice, Via Torino 155, 30172, Venice, Italy

^b A-Sense Research Group, University of Antwerp, Groenenborgerlaan 171, 2020, Antwerp, Belgium

^c NanoLab Center of Excellence, University of Antwerp, Groenenborgerlaan 171, 2020, Antwerp, Belgium

^d Department of Environmental Sciences, Informatic and Statistics, Ca' Foscari University of Venice, Via Torino 155, 30172, Venice, Italy

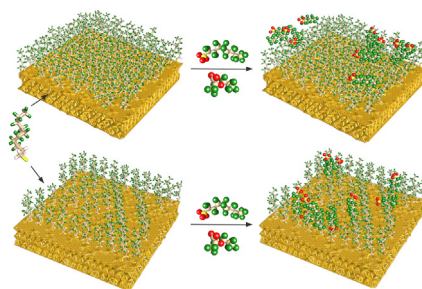
^e Department of Analytical Chemistry, Faculty of Chemistry, University of Vienna, Waehringer Strasse 38, A-1090 Vienna, Austria

^f European Centre for Living Technology (ECLT) Ca' Bottacin, 3911 Dorsoduro Calle Crosera, 30123, Venice, Italy

HIGHLIGHTS

- Fluorophilic interaction-based electrochemical strategies for fluorinated pollutants.
- Combining molecular dynamics simulations and electroanalysis in SAM studies.
- How PFAS exposure can alter different fluorinated SAM architectures?
- Fluorinated self-assembled monolayers applicability in PFAS sensor design.

GRAPHICAL ABSTRACT



ARTICLE INFO

Article history:

Received 6 January 2022

Received in revised form

10 March 2022

Accepted 16 March 2022

Keywords:

Self-assembled monolayer

Fluorosulfactant

per-fluoroalkyl substances

PFAS

2,3,3,3-Tetrafluoro-2-(heptafluoropropoxy)-

propanoate ammonium salt (HFPO-DA)

Perfluorooctanoic acid (PFOA)

Perfluorooctanesulfonic acid potassium salt

(PFOS)

Molecular dynamics simulations

Electrochemical sensing

ABSTRACT

There is an urgent need for sensing strategies to screen perfluoroalkyl substances (PFAS) in aqueous matrices. These strategies must be applicable in large-scale monitoring plans to face the ubiquitous use of PFAS, their wide global spread, and their fast evolution towards short-chain, branched molecules. To this aim, the changes in fluorinated self-assembled monolayers (SAM) with different architectures (pinholes/defects-free and with randomized pinholes/defects) were studied upon exposure to both long and short-chain PFAS. The applicability of fluorinated SAM in PFAS sensing was evaluated. Changes in the SAM structures were characterised combining electrochemical impedance spectroscopy and voltammetric techniques. The experimental data interpretation was supported by molecular dynamics simulations to gain a more in-depth understanding of the interaction mechanisms involved. Pinhole/defect-free fluorinated SAM were found to be applicable to long-chain PFAS screening within *switch-on* sensing strategy, while a *switch-off* sensing strategy was reported for screening of both short/long-chain PFAS. These strategies confirmed the possibility to play on fluorophilic interactions when designing PFAS screening methods.

© 2022 Elsevier B.V. All rights reserved.

* Corresponding author. Department of Molecular Sciences and Nanosystems, Ca' Foscari University of Venice, Via Torino 155, 30172, Venice, Italy.

E-mail address: giulia.moro@unive.it (G. Moro).

1. Introduction

Perfluoroalkyl substances (PFAS) represent a class of environmental toxicants widely applied in consumer products with harmful effects on our ecosystem and health [1–3]. Despite global widespread of PFAS pollution, industrial interests lead to continuous production and diversification of highly-fluorinated compounds. As a consequence, new analytical strategies to detect PFAS down to nanomolar or subnanomolar levels in environmental matrices, such as drinking waters, are urgently required [4,5]. Bio- and biomimetic sensors have shown promising results in PFAS determination even though most of these devices were conceived for the detection of a specific molecule and cannot monitor the whole class of these pollutants simultaneously [6–9]. Therefore, the design of class-selective sensing strategies would be instrumental to follow the fast evolution of these compounds and tackle all generations of PFAS, from long-chains (>C₈) to short ones (<C₇) [10,11]. It is worth noting that the hydrophobic-lipophilic properties of all generations of PFAS, which are of fundamental interest for industrial and household applications, depend mainly on their fluorinated tails. Thus, PFAS fluorinated chains (different in length and structure) can be used as a target for the development of PFAS screening strategies. To reach this aim, one needs to consider the high degree of fluorination of PFAS tails when selecting suitable molecular recognition layers. In particular, layers taking advantage from fluorine-fluorine (F–F) non-covalent interactions are of special interest as electrode modifiers for PFAS recognition. For instance, Niu et al. designed a colorimetric sensing strategy for perfluorinated compounds based on this type of interactions [12]. Aiming to provide new insights about possible PFAS sensing strategies, also Fang et al. described the fluorophilic interaction of C–F chains studying fluorinated self-assembled monolayers (SAM) exposed to perfluorooctanoic acid (PFOA) and perfluorooctanesulfonic acid (PFOS) [13]. The authors proved that SAM can be applied in PFOA sensing designing switch-on/off electrochemical platform [14]. These studies, together with a previous screening of anionic surfactants [15], provide a strong background to our study, which aims at testing and comparing different SAM architectures moving from traditional long-chain PFAS to the new generations of short-chain ones.

The use of organothiols SAM as sensing elements in electroanalytical applications was introduced in the 1990s [16]. Since then, these modifiers have been successfully applied in numerous electrochemical and impedimetric sensing platforms to measure pH and to detect metal ions, small molecules, biomolecules, and microorganisms [17,18]. SAM have made it possible to study surface-confined molecules and nanostructures at solid/liquid interfaces providing key information about the physicochemical properties of the latter (*i.e.*, wettability, catalytic effects, etc.) [19,20]. The adaptability and high compatibility of SAM with other molecular recognition elements can also find applications in the design of amplified recognition strategies to improve sensitivity, reproducibility, and speed of the resulting sensing devices [21,22].

In the design of SAM-based sensing strategies, the dynamic nature of organothiols SAM architectures needs to be taken into account [23]. SAM structural properties depend on the thiol chemical structure, on the conditions of the self-assembly process, and finally on the surface coverage along with the interactions (covalent/noncovalent) taking place at the SAM interface [24,25]. Alkanethiols on gold can result in highly ordered, pinhole/defect-free SAM (*ordered SAM* Fig. 1A) or SAM with randomly-positioned pinholes and/or defects (*unordered SAM* Fig. 1B) [26]. A pinhole is defined as a site on the substrate that is not covered by the monolayer, while a defect is formed when the thiol chain does not stand in an upright position [26].

The irregularities (pinholes/defects) in the SAM layer enable a direct electron transfer (ET) of the redox probe in solution. Therefore, *unordered SAM* are often combined with *switch-off* sensing strategies where increasing concentrations of the target lead to an increase in the order of the SAM structure and, as a consequence, to a decrease in the direct ET of the redox probe, as shown in Fig. 1B [3,4,5]. In these systems, the target molecules which are attracted by the SAM and the gold substrates tend to compete to insert in the pinholes/defects of the monolayer. This interaction mechanism was applied in the *switch-off* sensing strategy reported by Fang et al. to detect micromolar levels of PFOA via hydrophobic interactions with 6-(ferrocenyl)-hexanethiol SAM [14]. Noncovalent interactions (*i.e.*, Van der Waals, hydrogen bond, halogen bond, etc.) play a key role in SAM-based strategies and should be considered when designing new SAM recognition elements. These interactions can lead to structural changes in *unordered SAMs* that can be followed by electrochemistry and electrochemical impedance spectroscopy (EIS), as reported in this work.

When using different self-assembly conditions, the same alkanethiols with a chain length of more than nine carbon atoms can result in compact, well-organised and hydrophobic monolayers, which are modelled as pinhole- and defect-free SAMs [6,8,28]. These SAMs can isolate the electrode surface, blocking direct ET of electroactive species in solution allowing only for ET via tunnelling. In principle, this type of SAM can be integrated into *switch-on* sensing strategies, where the target molecules induce the formation of defects and pinholes, as in Fig. 1A. Through these irregularities the redox probe can undergo direct ET resulting in an increase of the faradic current signal.

The study of SAM sensing systems can be supported by molecular dynamics (MD) simulations that allow for predicting interaction mechanisms and estimating the non-covalent binding energies involved. Indeed, the use of MD simulations in the study of SAMs on inorganic surfaces is gaining importance [29–34] thanks to the continuous development of reliable and accurate empirical force fields [35–37]. Furthermore, beyond providing complementary input to interpret lab experiments, MD simulations and more generally molecular simulation methods can predict the preferential adsorption modes and phase segregation of alkanethiol mixtures on Au(111) slabs [37]. Vemparala and Karki have employed MD simulations to unravel the structural properties of alkanethiol SAMs as a function of temperature, lattice spacing, and molecular chain length [38]. Similarly, Devi used MD simulations to provide insight into the thermal and wetting behaviour of alkanethiol SAM on Au(111) surfaces, suggesting that it can be modified by altering the terminal functional group of the SAM chains [39]. Moreover, MD simulations underpinned the correlation between the chemical structures of functionalised alkanethiol SAMs on gold surfaces and their underlying molecular motion at the picosecond time scale, thus demonstrating how alkyl chain motions correlate with the dynamics of the head group [40]. Here, MD simulations have provided atomistic details of the interaction modes of fluorinated pinhole- and defect-free SAM architectures on Au(111) monolayers, thereby making it possible to separate the main driving forces from each other.

This work investigates the structural changes of different types of fluorinated SAM (namely 1H,1H,2H,2H-perfluorodecanethiol, FDT-SAM) upon exposure to long- and short-chain PFAS via electrochemical and impedance-based methods, the data analysis is supported by MD simulations. *Unordered* and *ordered* FDT-SAM were characterised via voltammetric techniques, electrochemical impedance spectroscopy (EIS) and infrared spectroscopy. For pinhole- and defect-free SAM, the ET kinetic constants were studied via EIS potential scan, whereas electrode surface coverage was estimated via linear sweep voltammetry (LSV). Different trends

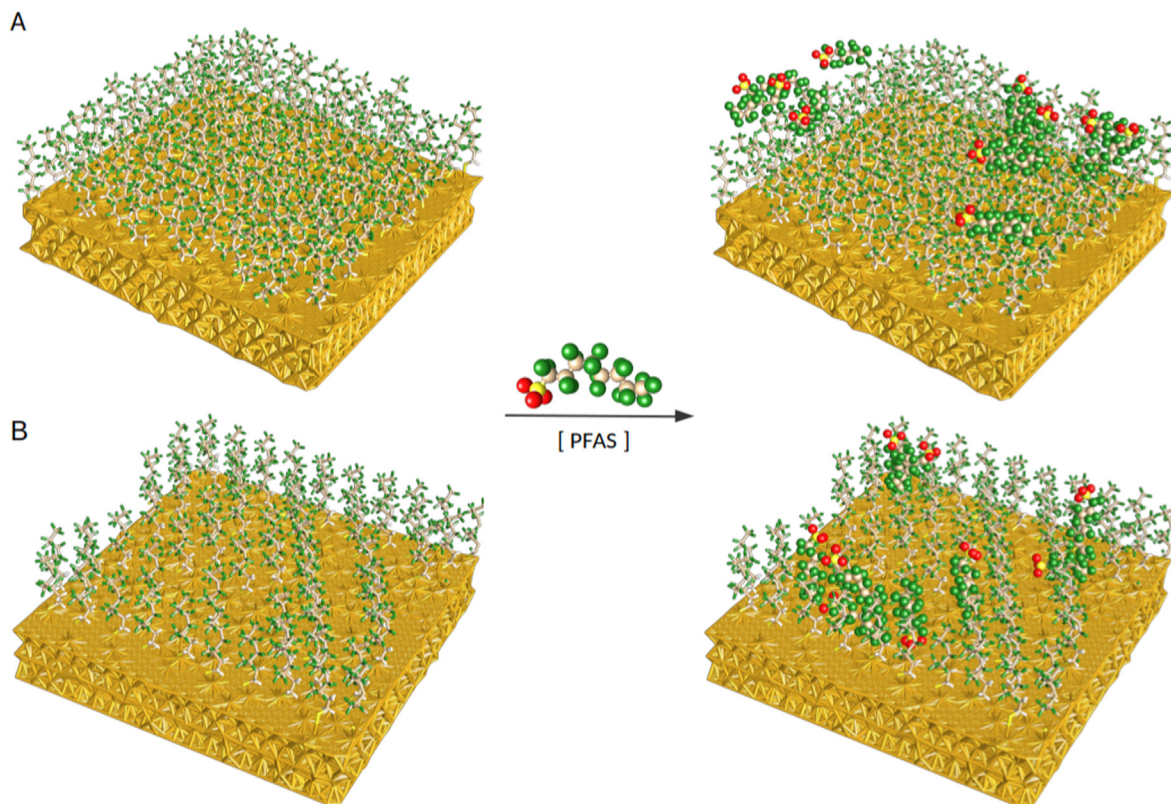


Fig. 1. Schematic of a possible *switch-on* (A) and *switch-off* (B) sensing strategies for the screening of PFAS based on fluorinated SAM at gold electrodes. The SAM are characterised by different architectures: an *ordered* one modelled as pinhole- and defect-free (A), and an *unordered* structure with pinholes and defects (B). Upon PFAS exposure, represented by the central arrow with PFOS molecule on top, *ordered* SAM might undergo the formation of pinholes/defects (followed by an increase in the redox probe currents, *switch-on*), while in *unordered* SAM structures PFAS molecules “fill the gaps” (with a decrease in the redox probe currents, *switch-off*). The colour code is as follows: gold = goldenrod; carbon = grey; sulphur = yellow; oxygen = red; fluorine = forest green; hydrogen = white. The images were generated and rendered using UCSF ChimeraX [27]. (For interpretation of the references to colour in this figure legend, the reader is referred to the Web version of this article.)

were observed under long- and short-chain exposure for *ordered* FDT-SAM, while FDT-SAM with pinholes and defects led to consistent response. These preliminary results suggest the applicability of FDT-SAM in sensing strategies for PFAS screening and the advantages of combining electrochemical and computational approaches.

2. Experimental section

2.1. Chemicals and materials

Potassium hydroxide, potassium chloride, potassium nitrate, hydrogen peroxide, potassium ferro(II/III)cyanide, sulfuric acid, dodecanethiol (DDT), 1H,1H,2H,2H-perfluorodecanethiol (FDT), 2,3,3,3-tetrafluoro-2-(heptafluoropropoxy)-propanoate ammonium salt (HFPO-DA), perfluorooctanoic acid (PFOA), perfluorooctanesulfonic acid potassium salt (PFOS), perfluoropentanoic acid (PFPA), perfluorohexanesulfonic acid (PFHxS) were purchased from Sigma Aldrich. All PFAS chemical structures are summarised in Fig. S.I. 1A Diamond slurry (3 μm), alumina powder (1 and 0.05 μm), nylon polishing cloths, micro-cloth PSA 2–7/8 were purchased from Buehler.

2.2. Protocols for SAM preparation

Prior to thiol chemisorption, polycrystalline gold disk electrodes (Au-DE) (geometric area 0.020 cm^2) were first treated by scanning 10 cyclic voltammetry (CV) cycles in 0.1 M KOH, in the potential window from -0.4 V to -1.6 V vs Ag/AgCl (KCl sat.), at a scan rate of

50 mV s^{-1} . All potentials are reported vs Ag/AgCl (KCl sat.). Second, Au-DE were mechanically polished for 2 min in a figure-eight pattern on Buehler microcloth with successive finer grades (15, 3 and 1 μm), diamond (3 μm) and alumina (1 and 0.05 μm), respectively, followed by sonication in ethanol/water (1:1) for 10 min. Third, the electrodes were treated by scanning 10 CV cycles in 1 M H_2SO_4 , in the potential window from -0.3 V to 1.7 V at a scan rate of 300 mV s^{-1} and followed by ten cycles in 0.5 M H_2SO_4 , 0.01 M KCl, in the potential window from 0 V to 1.7 V, at a scan rate of 300 mV s^{-1} . Finally, the potential was cycled between 0 and 1.7 V in 1 M H_2SO_4 until reaching stable CV.

Au-DE were modified with FDT and DDT-SAM by overnight (>14 h) or for 6 h incubation in 0.5 or 5 mM thiol solution in absolute ethanol at room temperature; these working conditions were selected depending on the desired SAM architecture. For highly *ordered* SAM, overnight incubation and an initial thiols concentration of 5 mM turned out ensured the formation of a stable monolayer with good blocking properties. For *unordered* SAM, the incubation time was reduced to 6 h and the thiols concentration was 0.5 mM. When using this second set of conditions, SAMs with a reproducible density of pinholes/defects were obtained as explained in Section 3.2. To assure reproducibility of both SAM architectures, the incubation steps were carried out at temperature/pressure-controlled conditions (room temperature and atmospheric pressure). Prior to use, modified Au-DE were rinsed to remove thiols adsorbed at the interface (nonspecific binding). Then, they were conditioned by soaking in 0.1 M KNO_3 for about 30 min.

2.3. Voltammetric and impedimetric study

Electrochemical measurements were carried out using a three-electrode cell setup: an Ag/AgCl (KCl sat.) reference electrode, a Pt coil counter electrode and SAM-modified Au-DE as working electrodes. All potentials are expressed vs Ag/AgCl (KCl sat.) electrode. CV and Square Wave Voltammetry (SWV) were carried out using different potentiostats/galvanostats: the CH model 660B and the Autolab Model 204 controlled by NOVA 1.1 software, respectively. CVs were recorded within the potential window from -0.2 to $+0.6$ V vs Ag/AgCl (KCl sat.) at a scan rate of 50 mV s^{-1} . DPV experiments were recorded in the potential window from -0.2 V to $+0.7$ V Ag/AgCl (KCl sat.), using the following parameters: potential increment of 0.002 V, amplitude of 0.025 V, pulse width of 0.025 s, sample width of 0.0125 s and pulse period of 0.05 s. Electrochemical impedance spectroscopy (EIS) measurements were carried out in the frequency range from 100 kHz to 0.1 (12 points per decade), with 0.01 V amplitude and an initial potential in the range from -0.4 to 0.6 V vs Ag/AgCl (KCl sat.). Measurements were carried out in 0.1 M KNO_3 , 1.0 mM of $\text{K}_3[\text{Fe}(\text{CN})_6]$, 1.0 mM $\text{K}_4[\text{Fe}(\text{CN})_6]$. To investigate the changes in SAM after PFAS exposure via EIS, SAM modified Au-DE were incubated in 100 nM aqueous solution of PFAS for 1 h and rinsed with distilled water afterwards; then, impedimetric measurements took place as described above. ZPlot and NOVA 2.1 software were used to fit impedimetric data. SAM changes after PFAS exposure were investigated via DPV in 0.1 M KNO_3 , 1.0 mM $\text{K}_4[\text{Fe}(\text{CN})_6]$, and increasing concentrations of PFAS (from 5 nM to 2 μM) by incubating the SAM modified Au-DE in the measurement solution for 30 min with each concentration prior to acquiring the voltammetric responses. As part of SAM characterisation, a desorption step was applied via linear sweep voltammetry (LSV) to estimate the electrode surface coverage. The desorption was carried out in KOH 0.05 M, in the potential range from -0.4 to -1.6 V (vs Ag/AgCl KCl sat.) at a scan rate of 50 mV s^{-1} . All experimental data were elaborated using Origin Pro 2020b.

2.4. ATR- FTIR control procedure

Infrared spectra were acquired in attenuated total reflection (ATR) mode with a Thermo Nicolet FTIR Nexus 750 spectrometer equipped with a Smart Endurance ATR accessory with a diamond crystal (survey area 0.75 mm^2). Spectra were recorded in the range from 400 to 4000 cm^{-1} with a resolution of 4 cm^{-1} , accumulating 256 scans. Three analyses were performed for each sample to ensure reproducibility of obtained spectra. Both bulk reagents and modified gold surfaces were analysed.

2.5. Simulation model setup

Molecular dynamics (MD) simulations were performed with Gromacs (v2018.7) [41]. The force field GolP-Charmm22* [42] was used for the gold slab. Parameters for the per-fluorinated alkylated compounds (FDT, PFOS, HFPO-DA, whose chemical structures are reported in Fig. S. I. 1A) were obtained from the Amber-compatible parameters of Gaff2 using Antechamber module of AmberTools [43,44], and then converting to Gromacs-like format using the acpipy.py script [45]. Charge optimization was performed using the AM1-BCC charge model [46,47]. All simulations took place in an aqueous medium by filling a rectangular box with the 3-site rigid TIP3P water model [48], see Fig. S. I. 1B-C. Potassium ions were subsequently added to account for the overall negative charge and achieve a concentration of 0.1 nM. Minimization of the solvent was performed keeping the positions of the organic moieties and of the gold atoms frozen.

MD simulations were performed on two PFAS, namely PFOS (long-chain PFAS) and HFPO-DA (short-chain PFAS). FDT molecules

were used to construct the SAM on a gold substrate (Fig. S.I. 1B). All the chemical structures of these compounds were drawn with the Avogadro software [49] and each of them was simulated in its deprotonated form. A gold (111) slab with a surface area of $(58.6 \times 60.9) \text{ \AA}^2$ and with a thickness of five atomic layers was used as substrate [50] (Fig. S.I. 1D). The gold slab was frozen throughout the simulations, while a harmonic restraining potential of $1000 \text{ kJ mol}^{-1} \text{ nm}^{-2}$ was applied to FDT-sulphur atoms in the case of the full SAM surface coverage simulations. In the case of the simulations mimicking the *unordered* SAM system, the restraining potential was also applied to the FDT heavy atoms, to prevent the molecules from lying down on the gold slab.

The base of the 3D simulation box was set equal to the surface of the gold substrate, while the z-component was set equal to 80.0 \AA . Two mirrored gold slabs, each modified with FDT-SAM, were hosted in the simulation box (Fig. S.I. 1D-F). The distance between the FDT molecules and the slabs, taken as the distance between the sulphur atom and the upper external layer of the substrate was set equal to 2.42 \AA , within the limit of Au-S covalent bond formation. The chemical structure of FDT was obtained from 1 ns of MD simulation, thereby optimizing the geometry. The additional FDT-SAM was added on the opposite side of the simulation box to increase the probability of sampling binding/interaction events (Fig. S.I. 1B-C). Finally, in order to keep the FDT-SAM molecular assembly fixed at the bottom and top of the simulation box, the FDT-sulphur atoms along with the gold substrate were restrained throughout the simulation timescale.

Two different SAM architectures were simulated, as summarised in Fig. S.I. 1E-F. In the first, (E), the *ordered* FDT-SAM was arranged so that 110 FDT molecules are placed perpendicularly to the substrate. The distance between these molecules, measured as the separation distance between their sulphur atoms, was set equal to 5.87 \AA , which is compatible with the occupation sites of the hexagonal lattice [23]. In this way, the substrate was uniformly and fully covered by FDT molecules, symbolizing a defect-free SAM. In the *unordered* one, (F), the substrate is partially covered by FDT molecules to mimic a pinhole scheme, with a surface coverage of 50% . This value was chosen in order to obtain a system that closely matches the experimental one, in which the surface coverage was estimated to be less than half the one of *ordered* SAM.

Subsequently, 10 PFOS or HFPO-DA molecules, initially placed in the middle of the simulation box, were added to both setups to investigate how they interact with the FDT-SAM monolayers and, eventually, modify the arrangement of these latter (see Fig. S.I. 1G).

A complementary setup including 10 target molecules (PFOS or HFPO-DA) and 10 FDT moieties was simulated in a periodic box of water embedding a single gold layer at one end of the simulation box. This setup allowed for estimating the non-covalent interactions along with visualizing the preferential binding modes upon binding to the Au (111) surface (see Fig. S.I. 1H).

2.6. Numerical protocol

MD simulations of at least 250 ns for each system were performed in the canonical NVT ensemble. However, it should be mentioned that the production runs were preceded by 5 ns equilibration in which the positions of all the heavy atoms were restrained. All parameters of the MD simulations were set according to [51]. Finally, the rigid-rod-dipole method for gold atom polarization was implemented as reported in [51]. The temperature was equilibrated to the reference value of 300 K using the Nose-Hoover thermostat [52,53] with a coupling constant of 0.2 ps. The leap-frog integrator with integration time step of 1 fs was used. The Particle Mesh Ewald summation was used to account for long-range electrostatics, with a real space cut-off of 10 \AA . Finally, simulations

used a periodic box and a force-switched cut-off starting at 9 Å and ending at 10 Å for the Van der Waals non-bonded interactions.

3. Results and discussion

3.1. Testing ordered fluorinated SAM applicability in switch-on sensing strategies

3.1.1. Electrochemical characterisation of SAM upon PFAS exposure

Pinhole/defects-free FDT-SAM were first characterised combining different electrochemical techniques and ATR-FTIR to assess the monolayer properties, especially the tunnelling electron transfer kinetics, in comparison with previously reported DDT-SAM [24], all details are reported in S.I. Section 1. The results confirmed the blocking properties of FDT monolayers. Afterwards, fluorinated SAM were tested as electrode modifiers for the development of switch-on sensing strategies using DPV to maximize the signal-to-noise ratio, as described in Fig. S.I. 2D. The changes in the structure of FDT and DDT-SAM after exposure to both long-chain and short-chain PFAS were studied (summary of PFAS chemical structures in Fig. S.I. 1A). We aimed at verifying whether, and eventually, to which extent hydrophobic, non-covalent interactions between SAM interface and PFAS molecules alter the SAM architectures (i.e., partial destabilization, compacting, etc.). For this preliminary test,

the long-chain PFAS considered were PFOA and PFOS, while the short-chain PFAS tested were PFHxS, HFPO-DA and PFPA.

Incubation with increasing concentrations of PFOS or PFOA (ranging from 50 to 1000 nM) was found to affect the insulating properties of FDT-SAM. Upon exposure to these long-chain PFAS, increasing oxidation currents were recorded at FDT-SAM modified electrodes, as shown in Fig. 2A–B. These results can be explained considering that once the SAM architecture is altered and pinholes/defects are formed, the redox probe can approach the electrode surface and undergo direct electron transfer. This results in current intensities much higher than those recorded when only electron tunneling occurs (Fig. S.I. 2D). These currents showed values lower than 10 nA in the potential region between 0.25 and 0.3 V vs Ag/AgCl sat. KCl. Currents of about 20 nA were observed after incubation with 50 nM PFOA/PFOS (Fig. 2A–B). Currents increased linearly with analyte concentrations in the range from 50 up to 1000 nM. For PFOA/PFOS concentrations higher than 1 μM one can observe a progressive decrease in current values. These changes in the FDT-SAM showed good reproducibility and were not observed during negative control experiments, (results summarised in Fig. S.I. 5A–F). No changes were recorded upon adding blank solutions (0.1 M KNO₃) for both FDT-SAM and DDT-SAM, used as control system. Incubating PFOS/PFOA at DDT-SAM using the same working conditions did not affect the insulating properties of the SAM

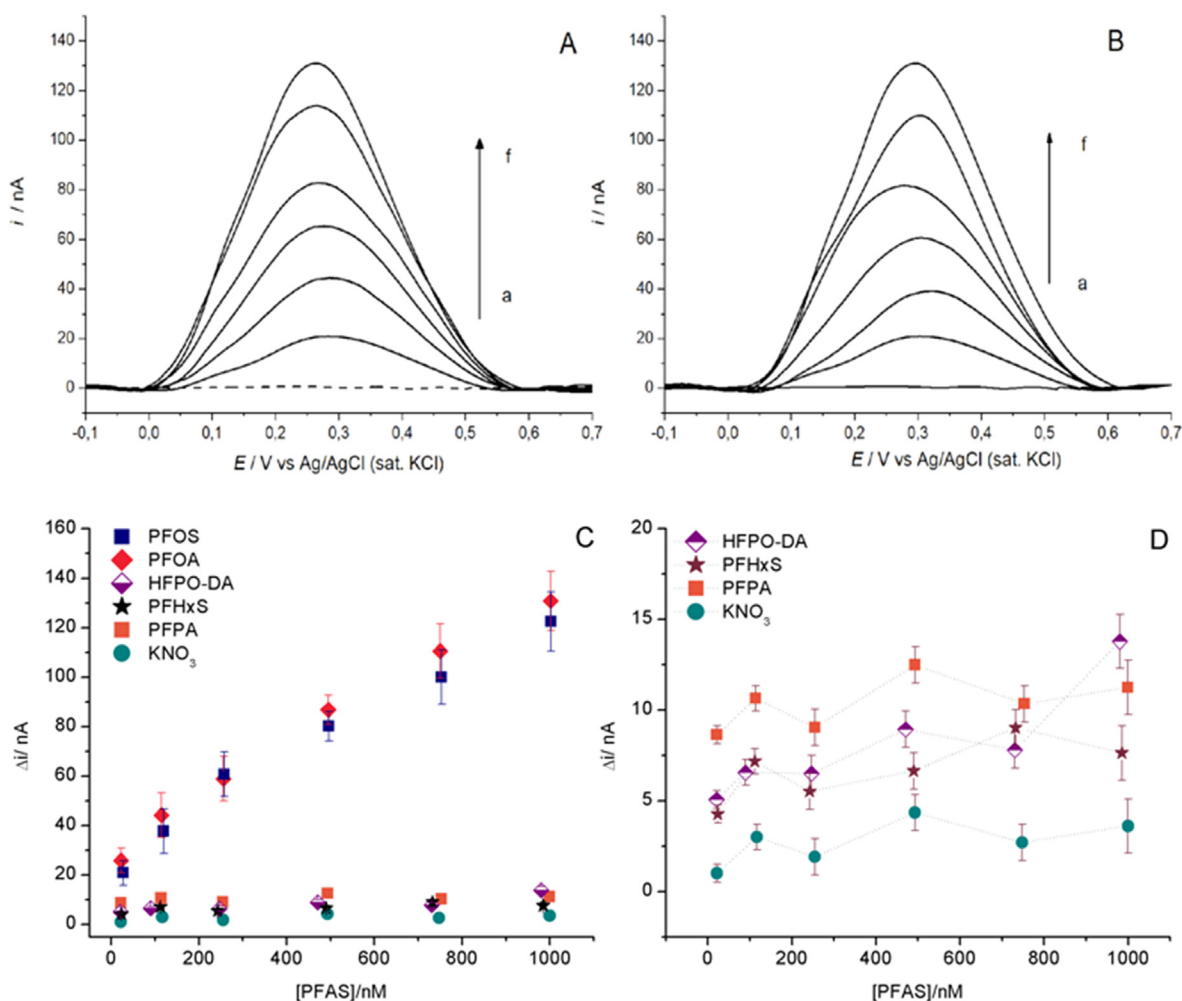


Fig. 2. (A–B) Representative voltammograms of FDT-SAM recorded via DPV upon exposure to increasing concentrations of PFOS (A) and PFOA (B), from 50 to 1000 nM (a to f), compared to their blanks (dotted line). (C–D) Plots of the peak current vs increasing concentrations of PFAS (PFOS, PFOA, HFPO-DA, PFHxS and PFPA) (C) and only short-chain PFAS, namely HFPO-DA, PFHxS and PFPA (D).

(results summarised in Fig. S.I. 5C–D). This experiment indirectly confirmed that the variations observed at FDT-SAM can be ascribed mainly to F–F interactions between the PFAS molecules and FDT tails.

The observations above are limited to long-chain PFAS: the incubation of short-chain PFAS, namely PFHxS, HFPO-DA and PFFA, did not lead to any recordable change in the FDT-SAM structure (Fig. S.I. 6). In Fig. 2C–D, the current values were reported as a function of different PFAS concentrations after blank subtraction at a fixed potential of 0.3 V vs Ag/AgCl (sat. KCl) and expressed as Δi . The variations observed after blank additions (0.1 M KNO₃) were found to be lower than 10 nA, thus Δi values of <10 nA were considered not meaningful in the present analysis.

Fig. 2C highlights that PFOS/PFOA exposure leads to changes in the FDT structure, which are linearly proportional to PFAS concentrations. The long-chain PFAS shows consistent behaviour, which differs fundamentally from the short-chain one. Indeed, PFHxS, HFPO-DA and PFFA do not alter the FDT-SAM structure in a significant way. Their Δi values are on average < 10 nA as shown in Fig. 2D. This comparison underlines that there are no clear trends. Even the exposure to relatively high concentrations of short-chain PFAS (>1000 nM) did not alter the blocking properties of FDT-SAM. Short-PFAS are potentially contributing to compact SAM structure by lying in the interfacial region. The relatively higher solubility of short-chain PFAS, as discussed in the following section, together with their shorter length might be responsible for the behaviour observed. Overall, PFHxS, HFPO-DA and PFFA show consistent trends. A similar behaviour was observed for DDT-SAM, again tested as a negative control.

The differences observed in FDT-SAM blocking properties upon exposure to long and short-chain PFAS cannot be simply explained by the fluorinated tail length. For this reason, prior to further apply FDT-SAM in PFOS/PFOA monitoring, it is necessary to elucidate the interactions involved. These results provide evidence that screening PFAS at pinholes/defects-free FDT-SAM via a switch-on strategy is not applicable to short-chain PFAS, but only to long-chain ones.

3.1.2. MD simulations vs experimental outcomes

MD simulations showed that both PFOS and HFPO-DA adhere to the FDT-SAM interface without altering the monolayer arrangement, as shown in Fig. 3. These arrangements are driven by an attractive force, rather than a repulsive one, as suggested by the negative values of the interaction energies observed.

To assess whether there is any difference between the affinities of the two target molecules, i.e., the short- and long-chain PFAS, with the SAM, we analyse MD simulations as follows: for each of the molecules, we compute the number of contacts between the target molecule atoms and the atoms of the SAM. We define two atoms to be in contact if their separation is within 0.6 nm (Fig. S.I. 7A–B). In turn, we deem the target molecule as (reversibly) bound to the SAM if its number of contacts is ≥ 16 for the short-chain HFPO-DA, and ≥ 27 for the long-chain PFOS (Fig. S.I. 7E–F). Finally, to extract the affinity to the SAM, we computed the average potential energy of the two interacting molecules when bound according to the above criterion. These energies were found to be -36 kJ/mol for the system with PFOS and -23 kJ/mol for the one with HFPO-DA, where non-interacting molecules would have zero

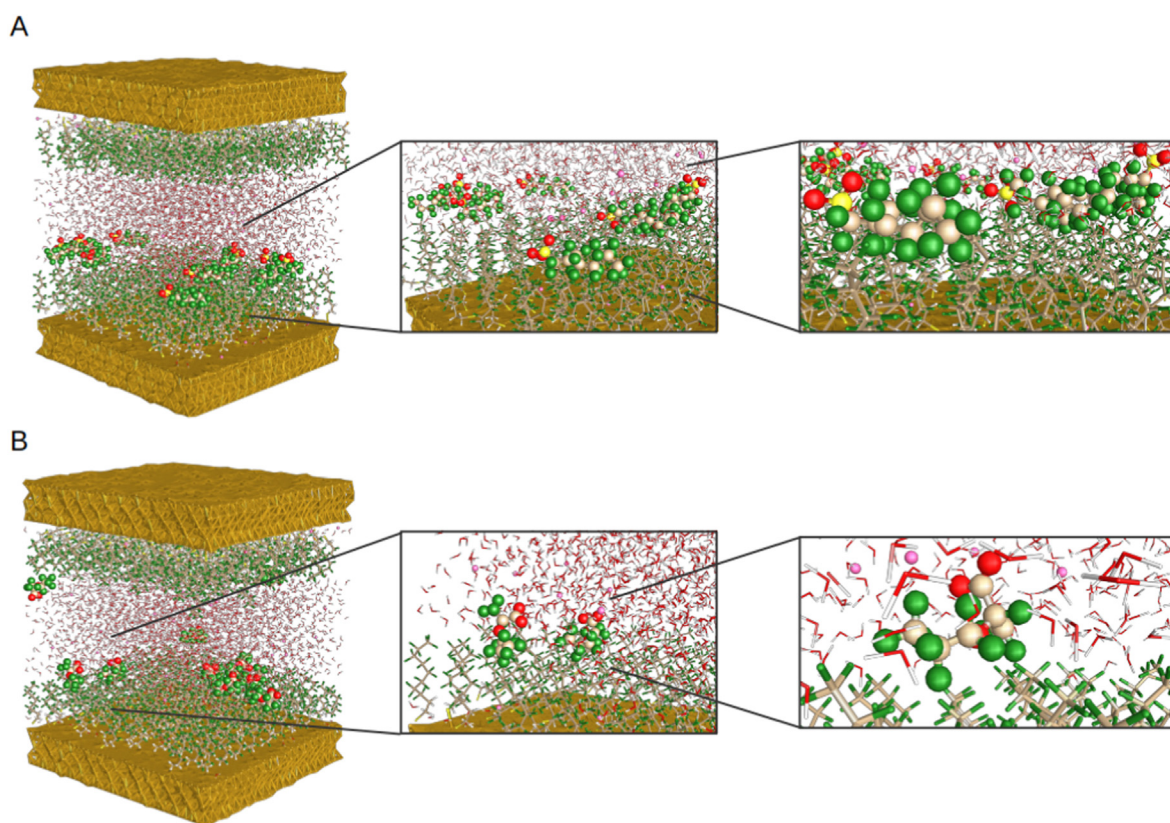


Fig. 3. Framework of the solvated MD simulations box with two gold substrates modified with an ordered FDT-SAM upon exposure to: (A) PFOS and (B) HFPO-DA. The close-up views of the middle and rightmost sides show an increased zoom in the interactions of molecules with the interfacial FDT-SAM. PFOS, HFPO-DA and potassium ions are drawn in van der Waals spheres, while FDT and gold substrates are shown in licorice representation. The colour code is as follows: gold = goldenrod; carbon = grey; sulphur = yellow; oxygen = red; fluorine = forest green; hydrogen = white; potassium = hot pink. The images were generated and rendered using UCSF ChimeraX [27]. (For interpretation of the references to colour in this figure legend, the reader is referred to the Web version of this article.)

interaction energy. We found that both targets display a negative interaction energy with the SAM monolayer, albeit the affinity of the long-chain PFOS being significantly (13 kJ/mol) more favourable.

This difference in PFOS/HFPO-DA behaviour can be explained considering the chemical structures of these pollutants and, as a consequence, their different physicochemical properties. According to Nixon et al., HFPO-DA is considered to be infinitely soluble in aqueous solutions with low adsorption potential and high mobility [54,55]. On the contrary, PFOS shows a solubility in pure water of about 680.0 mg/L at 25 °C in pure water according to 3M assessments, while in natural seawater a solubility of 12.4 mg/L at 22–23 °C was measured [56].

As a consequence of their chemical nature, PFOS molecules in aqueous solution will be strongly attracted by the fluorinated SAM and the gold substrate, as further discussed in Section 3.2. They will get involved in stable interactions with the SAM interfacial region, thereby increasing their number of contacts with the fluorinated surface. During this process, driven by an attractive force, the insertion of PFOS in the SAM arrangement might occur even though it was not clearly observed in our classical simulations. If we assume that similar events occur in the experimental setup, it would be possible to partially explain the results observed in the previous section. However, the MD simulations did not reveal any deep alterations of the FDT-SAM structure contrary to experimental data. The discrepancy observed suggests that the results reported in Section 3.1.1 might not be correlated to an alteration of the SAM structure caused by the exposure to PFOA/PFOS, but to other side-processes which destabilize the monolayer. Although further studies will be needed to elucidate this phenomenon, the results collected so far and the comparison between experimental and simulation data allow excluding the possibility to apply pinhole/defect-free FDT-SAM in screening even long-chain PFAS screening.

The scenario changes when one considers HFPO-DA: MD simulation and experimental data are fully consistent for this compound. Fig. 3 helps to explain why one does not observe changes in the current values upon HFPO-DA exposure in Section 3.1.1: the target molecules partially interact with the surface. The higher solubility of HFPO-DA compared to PFOS is responsible for the weaker attraction of this compound with the FDT-SAM interfacial region. The FDT-SAM structure is not altered and not even compacted by the interaction with short-chain PFAS. In this case, the MD simulations allowed for in-depth understanding of the underlying mechanisms: FDT/HFPO-DA attractive forces are not prevalent and HFPO-DA is involved in multiple equilibria (HFPO-DA/HFPO-DA, HFPO-DA/FDT interaction, etc.) which are strongly affected by the working conditions. Hence this part of the study can explain why such *ordered* SAM are not suitable for sensing low-chain PFAS.

However, these findings do not imply that fluorinated SAM with different architectures combined with other sensing strategies (different from *switch-on*) should not be considered. For this reason, the next section discusses a different FDT and DDT-SAM architecture.

3.2. Testing unordered fluorinated SAM applicability in switch-off sensing strategies

3.2.1. Electrochemical characterisation of SAM upon PFAS exposure

SAM with a controlled density of pinholes and defects are often used in *switch-off* sensing of small-organic molecules, as stated in Section 1. After having tested highly *ordered* SAM, the investigation of possible fluorinated modifiers for the design of PFAS sensors moved towards less-ordered monolayer arrangements with partial blocking properties. In the presence of such modifiers, electron

transfer can occur directly with no need to study the kinetics of other transfer processes, as in S.I. Section 1. FDT-SAM containing pinholes/defects can be obtained by lowering both initial thiol concentration and incubation time as described in Section 2.2. For the sake of simplicity these FDT-SAM will be referred to as *unordered* in this work. Such FDT-SAM obtained showed reproducible results after introducing suitable rinsing/soaking steps in 0.1 M KNO₃ solutions 2.2, which remove thiols that are not bound to the gold substrate. Voltammetric characterization of these FDT-SAM took place at the conditions described in Section 3.1. Such modifiers allow for direct ET via their pinholes/defects, as suggested by the well-defined redox process observable in the voltammograms of Fig. 4 A-B. The voltammetric parameters ($E_{1/2}$ and ΔE_p) agree very well with what is expected for a reversible one-electron redox process. Oxidation (Fig. 4B) results in a sharp Gaussian peak with $E_{pa} = +0.22$ V vs Ag/AgCl (sat. KCl) contrary to previous observations for *switch-on* FDT-SAM system, where broad oxidation peaks were recorded covering multiple processes. The Faradaic currents here are in the order of hundreds of nA confirming that even *unordered* FDT-SAM show obvious blocking properties (at a bare Au-DE these currents will be in the μ A range). Also, for this second FDT-SAM architecture, surface coverage was estimated via LSV resulting in an experimental value of 1.3 nmol cm⁻². Keeping in mind the above-mentioned considerations about the possible error factors of this methodology, it is still possible to compare *ordered* and *unordered* FDT-SAM systems qualitatively. This comparison suggests that for *unordered* SAM the surface coverage is less than half of the *ordered* one.

Fig. 4B shows a drop in the E_{pa} currents upon exposure to increasing concentrations of HFPO-DA (from 0.5 to 10 μ M), such a trend was observed for all PFAS tested. This first screening carried out in a wide range of PFAS concentrations confirm that it is possible to follow increasing PFAS concentration at *unordered* FDT-SAM; no signal saturation was observed in the range tested. The decreases in oxidation peak currents were first observed via CV and, then, via DPV (Fig. 4A–B).

The differences in oxidation peak currents at increasing PFOA/PFOS concentrations show a linear trend (linear fitting $R^2 > 0.98$), as reported in Fig. 5A. As a control experiment, FDT-modified Au-DE were incubated with KNO₃ to evaluate the possible alteration of the SAM upon successive incubations. The results clearly demonstrate that no meaningful variations occurred. Furthermore, adding the electrolyte solution did not lead to the trends observed upon incubating with the pollutants. Therefore, *unordered* FDT-SAM show a good stability. Changes in their blocking properties can be correlated with the presence and insertion of long-chain PFAS into their structure. The error bars, calculated from triplicate measurements, suggest good reproducibility of the results. PFOA insertion in pristine SAM was previously observed by Fang et al. using μ M concentrations of this pollutant [15]. The authors explained the tendency of PFOA to intercalate into SAM defects/pinholes by considering the formation of partial-micelles and its highly fluorinated nature, without elucidating the interactions (mainly attractive/repulsive forces). Therefore, one can assume that other short- and long-chain PFAS will also insert into monolayers, compacting them and thus increasing their blocking properties leading to meaningful decrease in probe oxidation currents. Such changes in FDT-SAM architectures allow one to detect PFOS and PFOA in the low nM range as well as μ M range (up to 10 μ M). Contrary to what was observed in Section 3.1, the results after incubation of long-chain and short-chain PFAS at *unordered* FDT-SAM show a consistent trend.

Incubating with increasing concentrations of PFHxS, HFPO-DA and PFFA leads to progressive decrease in probe oxidation current (Fig. 5B). The results suggest that also short-chain PFAS intercalate

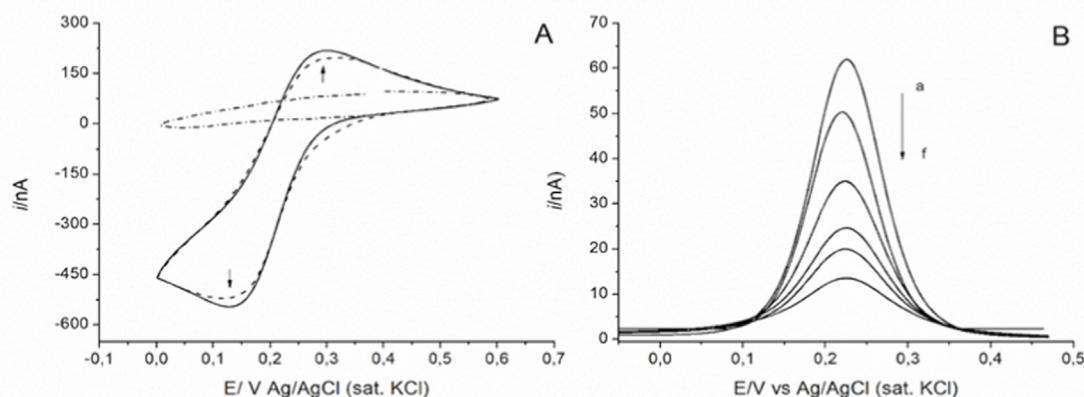


Fig. 4. (A) Cyclic voltammograms of *unsorted* FDT-SAM in 1.0 mM of $K_3[Fe(CN)_6]$, 1.0 mM $K_4[Fe(CN)_6]$ (solid line), 0.1 M KNO_3 aqueous solution (dotted line for the blank) and upon exposure to a 500 nM HFPO-DA solution (dashed line); inset: arrows pointing the changes in redox peak currents prior/after HFPO-DA incubation. (B) DPV of *unsorted* FDT-SAM in presence of the redox probe after incubation with increasing concentrations of HFPO-DA (0.0, 0.5, 1.5, 5.0, 7.5, 10.0 μM , from a to f). HFPO-DA was considered representative for both long- and short-chain PFAS.

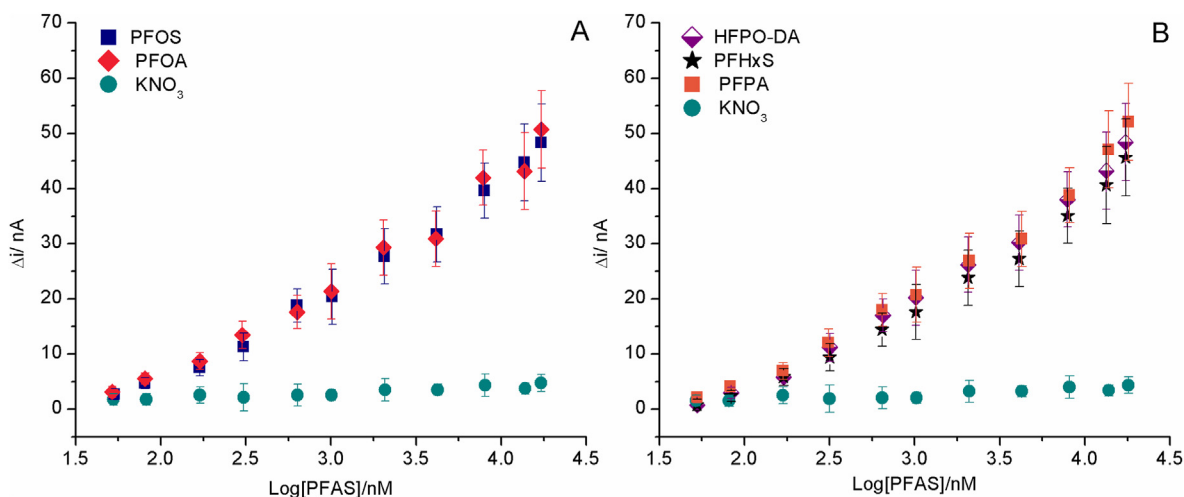


Fig. 5. Calibration plots of long- (A) and short- (B) chain PFAS after incubation at *unsorted* FDT-SAM. The changes in the peak currents are plotted versus the logarithm of the PFAS concentrations: PFOS and PFOA (A) and PFHxS/HFPO-DA/PFPA (B). In both plots, the electrolyte solution (KNO_3) serves as the blank, were included for comparison.

into FDT-SAM pinholes and defects, compacting the monolayer structure. Due to their different physicochemical properties (especially their increased solubility compared to long-chain PFAS), PFHxS, HFPO-DA and PFPA may have undergone interactions other than insertion. These findings confirm the possibility to apply FDT-SAM-based sensing to screen and estimate the total amount of both long- and short-chain PFAS in aqueous samples at nanomolar levels. However, this strategy needs to be further improved and optimised to fully match the strict regulation limits imposed by regional or national environmental agencies worldwide [57–59]. The current lack of detailed information on PFAS ecotoxicity resulted in the implementation of differing guidelines and action plans in the different countries making an international validation of the sensing strategy sensitivity rather impossible. For instance, the current environmental quality limits (EQLs) for PFOA drinking water prescribed by US EPA are about 70 ng L^{-1} ($\approx 0.17 \text{ nM}$), while the German Government allows for a maximum concentration of 100 ng L^{-1} ($\approx 0.24 \text{ nM}$) and the Australian Drinking Water Guidelines recommended values lower than 560 ng L^{-1} ($\approx 1.35 \text{ nM}$) [60,61]. In PFAS polluted sites, PFAS levels can be over one hundred times higher than the EQLs or maximum residue limits prescribed,

as for the Ruhr area (Germany) where Skutlarek et al. reported a PFOA concentrations up to 519 ng L^{-1} ($\approx 1.3 \text{ nM}$) in drinking water [62]. Our preliminary results suggest the possibility to screen PFAS in a wide concentration range (10^2 – 10^5 nM), further optimisations of the sensing platform will allow it to fulfil the regulation requirements and EQLs levels.

Comparing the data in Fig. 5A–B, one can see that the trends for PFOA/PFOS and PFHxS/HFPO-DA/PFPA are consistent. Further modifications of these monolayers might allow for obtaining intra-class selectivity. However, this is beyond the scope of this preliminary study. The consistency of PFAS interactions with FDT-SAM needed to be further explained from a molecular point of view. Furthermore, a complete series of negative control experiments in the study of *unsorted* FDT and DDT *unsorted* SAM in a meaningful way; trends observed at *unsorted* DDT-SAM after PFAS incubation differ from those at FDT-SAM (overview in Fig. S.I. 8). Once again, the crucial role of fluorophilic interactions was confirmed, as previously reported by Fang et al. [13]. Despite the growing number of studies regarding F-F interactions at the solid state (i.e. [63]), the experimental characterisation of these interaction in solution is still lacking.

3.2.2. MD simulations vs experimental outcomes

To better understand the mechanism of interaction of PFAS with FDT-SAM pinholes/defects, MD simulations were run considering an *unordered* monolayer. As for the previously simulated systems, 10 PFOS and 10 HFPO-DA molecules were considered as representative compounds for long-chain PFAS and short-chain PFAS, respectively. The gold slab was placed at the bottom of the simulation box, and its surface at the interface with the solvent was only 50% covered by FDT molecules, in order to mimic the pinholes in the fluorinated SAM architecture. As described in Section 3.1.3, an additional fluorinated SAM with the same characteristics as the former was added to the top of the simulation box to increase the probability of sampling more binding/interacting events.

During MD simulations of both systems, one can observe insertion of the targets into the FDT-SAM pinholes, as shown in the snapshots reported in Fig. 6. In the close-up look, the system in Fig. 6A shows that most of PFOS molecules fit the pinholes with the hydrophilic head group oriented towards the interfacial region of the FDT-SAM. Indeed, in these cases there is no way for them to lie on the gold substrate, probably due to their relatively linear and long chains that limit their conformational freedom once trapped in the FDT-SAM.

A similar behaviour is observed in Fig. 6B with HFPO-DA molecules filling SAM gaps. However, HFPO-DA hydrophilic head group are mostly pointing towards the gold substrate instead of facing the FDT-SAM/aqueous solution interface. This different orientation can be ascribed to the relatively short length of the HFPO-DA, and to the strong affinity of these fluorinated target molecules (i.e., PFOS and HFPO-DA) to the gold substrate. Indeed, different simulation

snapshots show that HFPO-DA tends to lie on the gold substrate in the case of sufficiently large pinholes.

To estimate non-covalent interaction energies (computed as Lennard-Jones and van der Waals interactions) of these target molecules with the gold substrate, a different simulation model setup was implemented. 10 FDT molecules and 10 target molecules (PFOS and HFPO-DA) were placed in solution in a periodic simulation box having only one gold substrate at one end.

The average energies obtained for a single molecule are equal to -86 kJ/mol for long-chain PFOS molecules, and to -57 kJ/mol for short-chain HFPO-DA molecules. These energies were calculated following the same procedure as described in Section 3.1.3, by determining the numbers of contact, and by considering only the energies corresponding to time windows where the number of contacts was greater than or equal to the chosen threshold (≥ 15 for the HFPO-DA molecules, and ≥ 23 for the PFOS molecules).

We further studied the affinity of both target moieties with *unordered* SAM with the same methods described in Section 3.1.3. The plots of the number of contacts (Fig. S.I. 9A-B) show that PFOS molecules can insert into the pinholes by forming more stable non-covalent bonds with the FDT molecules of the monolayer, than the bonds formed by the HFPO-DA counterpart. In this case, we set the threshold of the number of contacts ≥ 19 for the short-chain PFAS, and ≥ 28 for the long-chain PFAS, see Fig. S.I. 9E-F. The corresponding average interacting energies computed according to this threshold are equal to -51 kJ/mol for the system with PFOS and -38 kJ/mol for the one with HFPO-DA. Even in this case, the affinity of long-chain PFOS is significantly (13 kJ/mol) more favourable. However, it is worth noting that the HFPO-DA single

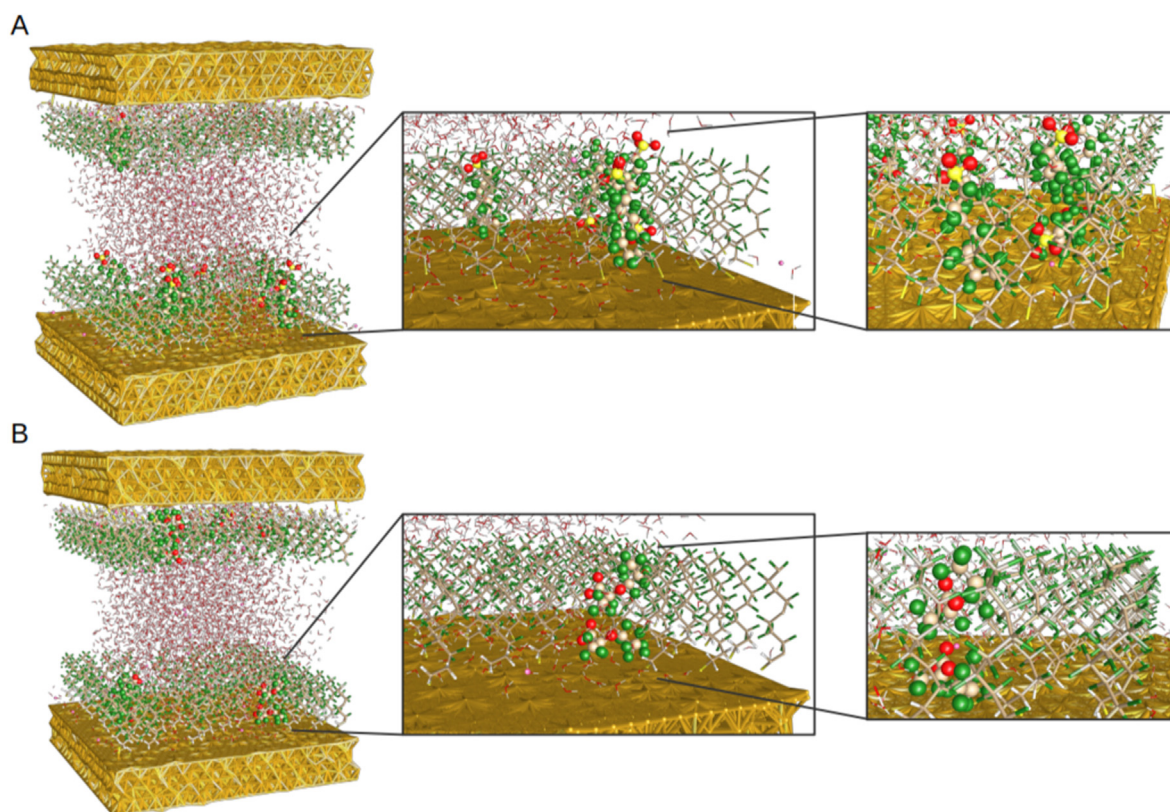


Fig. 6. Framework of the solvated MD simulations box with two gold substrates modified with an *unordered* SAM. FDT-SAM upon exposure to: (A) PFOS and (B) HFPO-DA. The close-up views of the middle and rightmost sides show an increased zoom in highlighting the orientation of PFAS molecules interacting with the interfacial FDT-SAM. PFOS, HFPO-A and potassium ions are drawn in van der Waals spheres, while FDT and gold substrates are shown in licorice representation. The colour code is as follows: gold = goldenrod; carbon = grey; sulphur = yellow; oxygen = red; fluorine = forest green; hydrogen = white; potassium = hot pink. The images were generated and rendered using UCSF ChimeraX [27]. (For interpretation of the references to colour in this figure legend, the reader is referred to the Web version of this article.)

molecules that form more stable bonds with FDT-SAM have energies of the same order of magnitude (-50 kJ/mol) as those determined by the PFOS system. Besides, the literature does not provide quantitative data for the interaction energy to compare with. Thus, the values reported herein should be taken with due care and likely be viewed as a general order of magnitude for PFAS interacting entities considered here in general, and fluoro-fluoro tails, in particular. Nonetheless, these values are consistent with those reported in Ref. [17,42] for small organic moieties adsorbed onto Au(111) monolayers.

In conclusion, FDT-SAM with pinholes/defects were found to be suitable for PFAS screening. The linear trends were observed in concentration range from 100 to 1000 nM. The sensitivity of these *switch-off* sensing strategies can be further improved with additional optimizations steps or combining FDT-SAM with other modifiers. The results described in this section proved the importance of a complete characterisation of the SAM modifiers, the need of a complete series of negative control experiments and the interest of supporting electrochemical data interpretation via MD simulations.

4. Conclusions

The changes in FDT-SAM with a pinholes/defects-free structure (*ordered SAM*) or randomized pinholes/defects architecture (*unordered SAM*) were studied upon long- and short-chain PFAS exposure. We aimed to evaluate fluorinated SAM applicability in the development of *switch-on* or *switch-off* sensing strategies for PFAS. The changes in the SAM structures were studied considering variations in the blocking properties of the monolayers via a combination of electrochemical impedance spectroscopy and voltammetry. Experimental data interpretation went hand in hand with molecular dynamics simulations for understanding the possible interaction mechanisms involved, especially fluorine-fluorine ones, in a more in-depth manner.

During the first part of the study, *ordered SAM* were investigated characterising their blocking properties (in particular, the kinetics of the electron tunneling) and surface coverage. These findings can be further applied in the design of *ordered* FDT-SAM for other sensing applications. Complete electrochemical and impedimetric characterisation serves this purpose. *Ordered* FDT-SAM were found to be unsuitable for PFAS screening because short-chain PFAS did not lead to any traceable change in SAM properties. Changes in the *ordered* FDT-SAM structures were observed for long-chain PFAS (PFOS and PFOA). However, the experimental results showed poor reproducibility. These data were not supported by MD simulations: those showed that all long- and short-chain PFAS should deposit at the FDT-SAM interface without altering its structure or intercalate. PFAS molecules were found to minimise their energy by arranging themselves at the monolayer/solution interface. Therefore, changes in current intensities recorded for PFOA/PFOS were ascribed to other side-phenomena; this type of fluorinated SAM architecture was not further considered for sensing applications.

Another FDT-SAM architecture (*unordered*) was tested in the second part of the study. Upon PFAS exposure, *unordered* FDT-SAM showed increased blocking properties enabling sensing increasing PFAS concentration from nM to low μ M range. This system turned out to be compatible with *switch-off* sensing strategy for both long- and short-chain PFAS screening. For this second FDT-SAM architecture, experimental data and MD simulations lead to the same conclusions. Hence, it was possible to confirm and elucidate the insertion process of PFAS molecules interacting with *unordered* SAM. This mechanism was previously proposed in hypotheses, but not described in a quantitative way (estimating energies) yet. Overall, the present work underlines the importance of: *i*)

characterizing and comparing different SAM architectures, *ii*) supporting interpretation of electrochemical data with MD simulations to describe the interactions involved, and *iii*) using a reference system to operate a complete series of negative controls (DDT-SAM) and evaluate the contributions expected (FDT-SAM, F-F interactions). In both parts of this preliminary study, negative controls played a key role: they allowed to indirectly prove that the interactions observed depend on the presence of a fluorinate monolayer and, as a consequence, can be defined as fluorophilic. The application of fluorophilic interactions in the design of PFAS recognition elements for the development of sensing strategies is promising. Based on these interactions, it is possible to realize a new generation of sensing platform for screening of PFAS (all generations) thus answering the urgent need for portable and rapid analytical tools for PFAS monitoring in waste waters. For this purpose, fluorinated SAM modifiers can be further combined with other electrode surface materials to enhance the sensitivity and develop original sensing devices.

CRediT authorship contribution statement

Giulia Moro: Conceptualization, Methodology, Writing – original draft, Project administration. **Cedrix J. Dongmo Fomthum:** Investigation. **Marco Spinaci:** Formal analysis, Methodology, Writing – original draft, Investigation, (, Formal analysis, Methodology, Writing – original draft, Writing – original draft, Reviewing and Editing. **Ettore Martini:** Investigation, Formal analysis, Methodology, Writing – original draft. **Dafne Cimino:** Formal analysis, Investigation, ATR-FTIR analysis. **Eleonora Balliana:** Formal analysis, Investigation, (ATR-FTIR analysis). **Peter Lieberzeit:** Writing – review & editing, Conceptualization, Reviewing and Editing. **Flavio Romano:** Writing – review & editing, Supervision. **Achille Giacometti:** Writing – review & editing. **Rui Campos:** Writing – review & editing, Conceptualization, Methodology, Supervision, Reviewing and Editing. **Karolien De Wael:** Writing – review & editing, Supervision, Conceptualization, Reviewing and Editing. **Ligia Maria Moretto:** Writing – review & editing, Supervision, Conceptualization, Reviewing and Editing.

Declaration of competing interest

The authors declare that they have no known competing financial interests or personal relationships that could have appeared to influence the work reported in this paper.

Acknowledgement

The computational resources were provided by the SCSCF multiprocessor cluster at the University Ca' Foscari of Venice. We further acknowledge the CINECA project HP10CGFUDT for the availability of high-performance computing resources through the ISCRA initiative. This work was supported by MIUR PRIN-COFIN2017 "Soft Adaptive Networks" (grant code 2017Z55KCW acknowledged to A.G.) and by Marie Skłodowska-Curie Actions (grant number 842219 acknowledged to R.C.).

Appendix A. Supplementary data

Supplementary data to this article can be found online at <https://doi.org/10.1016/j.aca.2022.339740>.

References

- [1] C. Lau, K. Anitole, C. Hodes, D. Lai, A. Pfahles-Hutchens, J. Seed, Perfluoroalkyl acids: a review of monitoring and toxicological findings, *Toxicol. Sci.* 99 (2007)

- 366–394, <https://doi.org/10.1093/toxsci/kfm128>.
- [2] M. Houde, J.W. Martin, R.J. Letcher, K.R. Solomon, D.C.G. Muir, Biological monitoring of polyfluoroalkyl substances: a review, *Environ. Sci. Technol.* 40 (2006) 3463–3473, <https://doi.org/10.1021/es052580b>.
- [3] J.N. Meegoda, J.A. Kewalramani, B. Li, R.W. Marsh, A review of the applications, environmental release, and remediation technologies of per- and polyfluoroalkyl substances, *Int. J. Environ. Res. Publ. Health* 17 (2020) 1–26, <https://doi.org/10.3390/ijerph17218117>.
- [4] D. Barceló, T. Ruan, Challenges and perspectives on the analysis of traditional perfluoroalkyl substances and emerging alternatives, *TrAC Trends Anal. Chem.* (Reference Ed.) 121 (2019) 2–3, <https://doi.org/10.1016/j.trac.2019.07.016>.
- [5] M. Al Amin, Z. Sobhani, Y. Liu, R. Dharmaraja, S. Chadalavada, R. Naidu, J.M. Chalker, C. Fang, Recent advances in the analysis of per- and polyfluoroalkyl substances (PFAS)—a review, *Environ. Technol. Innovat.* 19 (2020) 100879, <https://doi.org/10.1016/j.eti.2020.100879>.
- [6] M.W. Glasscott, K.J. Vannoy, R. Kazemi, M.D. Verber, J.E. Dick, μ -MIP: molecularly imprinted polymer-modified microelectrodes for the ultrasensitive quantification of GenX (HFPO-da) in river water, *Environ. Sci. Technol. Lett.* 7 (2020) 489–495, <https://doi.org/10.1021/acs.estlett.0c00341>.
- [7] K.L. Rodriguez, J.H. Hwang, A.R. Esfahani, A.H.M.A. Sadmani, W.H. Lee, Recent developments of PFAS-detecting sensors and future direction: a review, *Micromachines* 11 (2020), <https://doi.org/10.3390/mi11070667>.
- [8] G. Moro, K. De Wael, L.M. Moretto, Challenges in the electrochemical (bio) sensing of nonelectroactive food and environmental contaminants, *Curr. Opin. Electrochem.* 16 (2019) 57–65, <https://doi.org/10.1016/j.coelec.2019.04.019>.
- [9] G. Moro, D. Cristofori, F. Bottari, E. Cattaruzza, K. De Wael, L.M. Moretto, Redesigning an electrochemical MIP sensor for PFOS: Practicalities and pitfalls, *Sensors* 19 (20) (2019) 4433, <https://doi.org/10.3390/s19204433>.
- [10] Z. Wang, J. DeWitt, C.P. Higgins, I.T. Cousins, Correction to “A never-ending story of per- and polyfluoroalkyl substances (PFAS)?” *Environ. Sci. Technol.* 52 (2018) 3325, <https://doi.org/10.1021/acs.est.8b00599>.
- [11] R.C. Buck, J. Franklin, U. Berger, J.M. Conder, I.T. Cousins, P. De Voogt, A.A. Jensen, K. Kannan, S.A. Mabury, S.P.J. van Leeuwen, Perfluoroalkyl and polyfluoroalkyl substances in the environment: terminology, classification, and origins, *Integr. Environ. Assess. Manag.* 7 (2011) 513–541, <https://doi.org/10.1002/ieam.258>.
- [12] H. Niu, S. Wang, Z. Zhou, Y. Ma, X. Ma, Y. Cai, Sensitive colorimetric visualization of perfluorinated compounds using poly(ethylene glycol) and perfluorinated thiols modified gold nanoparticles, *Anal. Chem.* 86 (2014) 4170–4177, <https://doi.org/10.1021/acs.4c03406d>.
- [13] C. Fang, Z. Sobhani, M. Megharaj, R. Naidu, Electrochemical proof of fluorophilic interaction among fluoro-carbon chains, *Electroanalysis* 30 (2018) 2349–2355, <https://doi.org/10.1002/elan.201800190>.
- [14] C. Fang, M. Megharaj, R. Naidu, Electrochemical switch on-off response of a self-assembled monolayer (SAM) upon exposure to per fluoroctanoic acid (PFOA), *J. Electroanal. Chem.* 785 (2017) 249–254, <https://doi.org/10.1016/j.jelechem.2016.12.040>.
- [15] C. Fang, M. Megharaj, R. Naidu, Electrochemical studies on self-assembled monolayer (SAM) upon exposure to anionic surfactants: PFOA, PFOS, SDS and SDBS, *Electroanalysis* 29 (2017) 2155–2160, <https://doi.org/10.1002/elan.201700108>.
- [16] D. Mandler, S. Kraus-Ophir, Self-assembled monolayers (SAMs) for electrochemical sensing, *J. Solid State Electrochem.* 15 (2011) 1–24, <https://doi.org/10.1007/s10008-011-1493-6>.
- [17] R. Campos, R. Katakay, Electron transport in supported and tethered lipid bilayers modified with bioelectroactive molecules, *J. Phys. Chem. B* 116 (2012) 3909–3917, <https://doi.org/10.1021/jp209772u>.
- [18] M. Singh, N. Kaur, E. Comini, The role of self-assembled monolayers in electronic devices, *J. Mater. Chem. C* 8 (2020) 3938–3955, <https://doi.org/10.1039/D0TC00388C>.
- [19] Y.F. Xing, S.F.Y. Li, A.K.H. Lau, S.J. O’Shea, Electrochemical impedance spectroscopy study of mixed thiol monolayers on gold, *J. Electroanal. Chem.* 583 (2005) 124–132, <https://doi.org/10.1016/j.jelechem.2005.05.010>.
- [20] Y.S. Shon, R. Colorado, C.T. Williams, C.D. Bain, T.R. Lee, Low-density self-assembled monolayers on gold derived from chelating 2-monoalkylpropane-1,3-dithiols, *Langmuir* 16 (2000) 541–548, <https://doi.org/10.1021/la981698l>.
- [21] H. Sahalov, B. O’Brien, K.J. Stebe, K. Hristova, P.C. Searson, Influence of applied potential on the impedance of alkanethiol SAMs, *Langmuir* 23 (2007) 9681–9685, <https://doi.org/10.1021/la701398u>.
- [22] P. Diao, M. Guo, D. Jiang, Z. Jia, X. Cui, D. Gu, R. Tong, B. Zhong, Fractional coverage of defects in self-assembled thiol monolayers on gold, *J. Electroanal. Chem.* 480 (2000) 59–63, [https://doi.org/10.1016/S0022-0728\(99\)00445-3](https://doi.org/10.1016/S0022-0728(99)00445-3).
- [23] O. Zenasni, A.C. Jamison, T.R. Lee, The impact of fluorination on the structure and properties of self-assembled monolayer films, *Soft Matter* 9 (2013) 6356–6370, <https://doi.org/10.1039/C3SM00054K>.
- [24] F.A. Aguiar, R. Campos, C. Wang, R. Jitchati, A.S. Batsanov, M.R. Bryce, R. Katakay, Comparative electrochemical and impedance studies of self-assembled rigid-rod molecular wires and alkanethiols on gold substrates, *Phys. Chem. Chem. Phys.* 12 (2010) 14804–14811, <https://doi.org/10.1039/c005402j>.
- [25] H.O. Finklea, Consequences of a potential-dependent transfer coefficient in ac voltammetry and in coupled electron-proton transfer for attached redox couples, *J. Electroanal. Chem.* 495 (2001) 79–86, [https://doi.org/10.1016/S0022-0728\(00\)00399-5](https://doi.org/10.1016/S0022-0728(00)00399-5).
- [26] Y.F. Xing, S.J. O’Shea, S.F.Y. Li, Electron transfer kinetics across a dodecanethiol monolayer self assembled on gold, *J. Electroanal. Chem.* 542 (2003) 7–11, [https://doi.org/10.1016/S0022-0728\(02\)01440-7](https://doi.org/10.1016/S0022-0728(02)01440-7).
- [27] E.F. Pettersen, T.D. Goddard, C.C. Huang, G.S. Couch, D.M. Greenblatt, E.C. Meng, T.E. Ferrin, UCSF Chimera—a visualization system for exploratory research and analysis, *J. Comput. Chem.* 25 (2004) 1605–1612, <https://doi.org/10.1002/jcc.20084>.
- [28] H.O. Finklea, S. Avery, M. Lynch, T. Furttsch, Blocking oriented monolayers of alkyl mercaptans on gold electrodes, *Langmuir* 3 (1987) 409–413, <https://doi.org/10.1021/la00075a024>.
- [29] J. Hautman, M.L. Klein, Simulation of a monolayer of alkyl thiol chains, *J. Chem. Phys.* 91 (1989) 4994–5001, <https://doi.org/10.1063/1.457621>.
- [30] A. Ulman, J.E. Eilers, N. Tillman, Packing and molecular orientation of alkanethiol monolayers on gold surfaces, *Langmuir* 5 (1989) 1147–1152, <https://doi.org/10.1021/la00089a003>.
- [31] B. Rai, S. P. C.P. Malhotra, Pradip, K.G. Ayappa, Molecular dynamic simulations of self-assembled alkythiolate monolayers on an Au(111) surface, *Langmuir* 20 (2004) 3138–3144, <https://doi.org/10.1021/la0357256>.
- [32] J. Wen, W. Li, S. Chen, J. Ma, Simulations of molecular self-assembled monolayers on surfaces: packing structures, formation processes and functions tuned by intermolecular and interfacial interactions, *Phys. Chem. Chem. Phys.* 18 (2016) 22757–22771, <https://doi.org/10.1039/C6CP01049K>.
- [33] T. Utesch, M. Sezer, I.M. Weidinger, M.A. Mroginski, Adsorption of sulfite oxidase on self-assembled monolayers from molecular dynamics simulations, *Langmuir* 28 (2012) 5761–5769, <https://doi.org/10.1021/la205055g>.
- [34] P.K. Ghorai, S.C. Glotzer, Molecular dynamics simulation study of self-assembled monolayers of alkanethiol surfactants on spherical gold nanoparticles, *J. Phys. Chem. C* 111 (2007) 15857–15862, <https://doi.org/10.1021/jp0746289>.
- [35] V.P. Raut, M.A. Agashe, S.J. Stuart, R.A. Latour, Molecular dynamics simulations of Peptide–Surface interactions, *Langmuir* 21 (2005) 1629–1639, <https://doi.org/10.1021/la047807f>.
- [36] F. Iori, R. Di Felice, E. Molinari, S. Corni, GoIP: an atomistic force-field to describe the interaction of proteins with Au(111) surfaces in water, *J. Comput. Chem.* 30 (2009) 1465–1476, <https://doi.org/10.1002/jcc.21165>.
- [37] P. Bhadra, S.W.I. Siu, Comparison of biomolecular force fields for alkanethiol self-assembled monolayer simulations, *J. Phys. Chem. C* 121 (2017) 26340–26349, <https://doi.org/10.1021/acs.jpcc.7b08092>.
- [38] S. Vemparala, B.B. Karki, R.K. Kalia, A. Nakano, P. Vashishta, Large-scale molecular dynamics simulations of alkanethiol self-assembled monolayers, *J. Chem. Phys.* 121 (2004) 4323–4330, <https://doi.org/10.1063/1.1775779>.
- [39] J. Meena Devi, A simulation study on the thermal and wetting behavior of alkane thiol SAM on gold (111) surface, *Prog. Nat. Sci. Mater. Int.* 24 (2014) 405–411, <https://doi.org/10.1016/j.pnsc.2014.06.009>.
- [40] C. Yan, R. Yuan, W.C. Pfalzgraff, J. Nishida, L. Wang, T.E. Markland, M.D. Fayer, Unraveling the dynamics and structure of functionalized self-assembled monolayers on gold using 2D IR spectroscopy and MD simulations, *Proc. Natl. Acad. Sci. Unit. States Am.* 113 (2016) 4929, <https://doi.org/10.1073/pnas.1603080113>. LP – 4934.
- [41] M.J. Abraham, T. Murtola, R. Schulz, S. Páll, J.C. Smith, B. Hess, E. Lindahl, Gromacs: high performance molecular simulations through multi-level parallelism from laptops to supercomputers, *SoftwareX* 1–2 (2015), <https://doi.org/10.1016/j.softx.2015.06.001>.
- [42] L.B. Wright, P.M. Rodger, S. Corni, T.R. Walsh, GoIP-Charmm, First-principles based force fields for the interaction of proteins with Au(111) and Au(100), *J. Chem. Theor. Comput.* 9 (2013) 1616–1630, <https://doi.org/10.1021/ct301018m>.
- [43] J. Wang, R.M. Wolf, J.W. Caldwell, P.A. Kollman, D.A. Case, Development and testing of a general amber force field, *J. Comput. Chem.* 25 (2004) 1157–1174, <https://doi.org/10.1002/jcc.20035>.
- [44] J. Wang, W. Wang, P.A. Kollman, D.A. Case, Automatic atom type and bond type perception in molecular mechanical calculations, *J. Mol. Graph. Model* 25 (2006) 247–260, <https://doi.org/10.1016/j.jmgm.2005.12.005>.
- [45] A.W. Sousa da Silva, W.F. Vranken, AcPyPe - AnteChamber PYthon parser interface, *BMC Res. Notes* 5 (2012) 367, <https://doi.org/10.1186/1756-0500-5-367>.
- [46] A. Jakalian, B.L. Bush, D.B. Jack, C.I. Bayly, Fast, efficient generation of high-quality atomic charges. AM1-BCC model: I. Method, 20000130, *J. Comput. Chem.* 21 (2000) 132–146, [https://doi.org/10.1002/\(SICI\)1096-987X, 21:2<132::AID-JCC5>3.0.CO;2-P](https://doi.org/10.1002/(SICI)1096-987X, 21:2<132::AID-JCC5>3.0.CO;2-P).
- [47] A. Jakalian, D.B. Jack, C.I. Bayly, Fast, efficient generation of high-quality atomic charges. AM1-BCC model: II. Parameterization and validation, *J. Comput. Chem.* 23 (2002) 1623–1641, <https://doi.org/10.1002/jcc.10128>.
- [48] W.L. Jorgensen, J. Chandrasekhar, J.D. Madura, R.W. Impey, M.L. Klein, Comparison of simple potential functions for simulating liquid water, *J. Chem. Phys.* 79 (1983) 926–935, <https://doi.org/10.1063/1.445869>.
- [49] M.D. Hanwell, D.E. Curtis, D.C. Lonie, T. Vandermeersch, E. Zurek, G.R. Hutchison, Avogadro: an advanced semantic chemical editor, visualization, and analysis platform, *J. Cheminf.* 4 (2012) 17, <https://doi.org/10.1186/1758-2946-4-17>.
- [50] J.-A. Huang, M.Z. Mousavi, G. Giovannini, Y. Zhao, A. Hubarevich, M.A. Soler, W. Rocchia, D. Garoli, F. De Angelis, Multiplexed discrimination of single amino acid residues in polypeptides in a single SERS hot spot, *Angew. Chem. Int. Ed.* 59 (2020) 11423–11431, <https://doi.org/10.1002/anie.202000489>.
- [51] L.B. Wright, P.M. Rodger, T.R. Walsh, S. Corni, First-principles-based force field

- for the interaction of proteins with Au(100)(5 × 1): an extension of GoIP-CHARMM, *J. Phys. Chem. C* 117 (2013) 24292–24306, <https://doi.org/10.1021/jp4061329>.
- [52] S. Nosé, A molecular dynamics method for simulations in the canonical ensemble, *Mol. Phys.* 52 (1984) 255–268, <https://doi.org/10.1080/00268978400101201>.
- [53] W.G. Hoover, Canonical dynamics: equilibrium phase-space distributions, *Phys. Rev.* 31 (1985) 1695–1697, <https://doi.org/10.1103/PhysRevA.31.1695>.
- [54] P.D. Willard, B. Nixon, B.S. Frank, J. Lezotte, Determination of the Water Solubility and Vapor Pressure of H-28308, Dupont-24129, U.S. EPA Product Properties Test Guidelines, 2008.
- [55] R.A. Hoke, B.D. Ferrell, T.L. Sloman, R.C. Buck, L.W. Buxton, Aquatic hazard, bioaccumulation and screening risk assessment for ammonium 2,3,3,3-tetrafluoro-2-(heptafluoropropoxy)-propanoate, *Chemosphere* 149 (2016) 336–342, <https://doi.org/10.1016/j.chemosphere.2016.01.009>.
- [56] D. Brooke, A. Footitt, T. Nwaogu, Environmental Risk Evaluation Report: Perfluorooctanesulphonate (PFOS), 2004. https://www.gov.uk/government/uploads/system/uploads/attachment_data/file/290857/scho1009brbl-e-e.pdf.
- [57] N.M. Brennan, A.T. Evans, M.K. Fritz, S.A. Peak, H.E. von Holst, Trends in the regulation of per- and polyfluoroalkyl substances (PFAS): a scoping review, *Int. J. Environ. Res. Publ. Health* 18 (2021), <https://doi.org/10.3390/ijerph182010900>.
- [58] R. Naidu, P. Nadebaum, C. Fang, I. Cousins, K. Pennell, J. Conder, C.J. Newell, D. Longpré, S. Warner, N.D. Crosbie, A. Surapaneni, D. Bekele, R. Spiese, T. Bradshaw, D. Slee, Y. Liu, F. Qi, M. Mallavarapu, L. Duan, L. McLeod, M. Bowman, B. Richmond, P. Srivastava, S. Chadalavada, A. Umeh, B. Biswas, A. Barclay, J. Simon, P. Nathanail, Per- and poly-fluoroalkyl substances (PFAS): current status and research needs, *Environ. Technol. Innovat.* 19 (2020) 100915, <https://doi.org/10.1016/j.eti.2020.100915>.
- [59] W.S. Dean, H.A. Adejumo, A. Caiati, P.M. Garay, A.S. Harmata, L. Li, E.E. Rodriguez, S. Sundar, A framework for regulation of new and existing PFAS by EPA, *J. Sci. Policy Gov* 16 (2020).
- [60] G.M. Sinclair, S.M. Long, O.A.H. Jones, What are the effects of PFAS exposure at environmentally relevant concentrations? *Chemosphere* 258 (2020) 127340, <https://doi.org/10.1016/j.chemosphere.2020.127340>.
- [61] National Health and Medical Research Council, Australian Drinking Water Guidelines 6 Version 3.7 Updated January 2022, 2022.
- [62] D. Skutlarek, M. Exner, H. Färber, Perfluorinated surfactants in surface and drinking waters, *Environ. Sci. Pollut. Res. Int.* 13 (2006) 299–307, <https://doi.org/10.1065/espr2006.07.326>.
- [63] C. Carrillo-Carrion, M. Atabakhshi-Kashi, M. Carril, K. Khajeh, W.J. Parak, Taking advantage of hydrophobic fluorine interactions for self-assembled quantum dots as a delivery platform for enzymes, *Angew. Chem. Int. Ed.* 57 (2018) 5033–5036, <https://doi.org/10.1002/anie.201801155>.